Chapter 20 – EXPERIMENTAL INVESTIGATIONS ON THE VFE-2 CONFIGURATION AT ONERA, FRANCE

by

Ovide Rodriguez

20.1 NOTATIONS

U	velocity
u, v, w	components of U in (ξ,η,ζ) reference frame
U_∞	freestream velocity
U_1	velocity component in a plan parallel to the wing ($U_1^2 = u^2+v^2$)
ω_R	vorticity
ϕ	Euler angle in rotation around x-axis
C_Y	lateral force coefficient
C_N	yaw moment coefficient

20.2 INTRODUCTION

Although the flow topology over high sweep delta wing has been extensively studied and is now reasonably well understood [20-1], [20-2], [20-3], [20-4], a complete knowledge of the influence of the vortical flow on the obstacle generating it, and in particular of the local induced unsteady effects, is to be acquired for moderated and high incidences. Furthermore, the CFD solutions for rounded leading edges did not well predict the measured surface-pressures and some improvements are still needed on the prediction of unsteady effects. Therefore there is a significant need to establish complementary data bases allowing to focus mainly on the unsteady flow properties, both on the obstacle and in the flowfield for which available data are less documented. As a consequence CFD prediction of these flows should be improved.

Present works were carried out within the RTO AVT-113-VFE2 framework entitled 'Understanding and Modelling Vortical Flows to Improve the Technology Readiness Level for Military Aircraft' which aimed at a better understanding of the vortical flow physics, at completing existing data bases and improving their prediction by CFD. They are based on using a unique 65° symmetrical delta wing geometry common for all members of the task group. This delta wing model can be equipped with various leading edges ranging from sharp to rounded. It has already been tested in NTF and LTPT NASA wind tunnels over a wide range of Reynolds numbers, Mach numbers and angles of attack. Results are available in a pre-existent data set [20-5].

This chapter presents the ONERA experimental contribution to VFE-2, restricted to low speed tests ($Re_{mac} = 10^6$, M = 0.133) carried out at the Lille center, in the L1 ONERA wind tunnel:

- Steady pressure measurements on the obstacle with the model previously tested in LTPT and lent by NASA to ONERA, in order to validate the tests in L1.
- Aerodynamic forces and moments measurement by using a gauge balance, what had not been done up to now with the NASA model, especially for the drag.

- Characterisation of the velocity field by PIV when the vortex breakdown point is located on the obstacle approximately at mi-cord.

Experiments were conducted both for 'sharp' and 'medium' leading edges. The NASA model tested in LTPT is provided with numerous static pressure taps. Connections are made with nickel tubes which length and stiffness are not appropriate to a balance use under acceptable uncoupling conditions. So, two resin one-piece reproductions of the NASA models were manufactured at ONERA fitted out with a 'sharp' and a 'medium' leading edge respectively. Aerodynamic forces and moments and velocity fields by PIV were recorded with these models. Within the framework of the RTO AVT-113 Group these two models have been lent by ONERA to Tubitak-Sage (Turkey). Tests have been performed during three different campaigns. Tests using the NASA model were conducted in solid walls configuration so as to ensure boundary conditions as similar as possible to LTPT ones, and were restricted to the measurement of static pressure distributions on the obstacle. On the other hand tests using the ONERA models were performed for different boundary conditions, i.e. in solid walls and in open jet tunnel. In solid walls forces were measured and the velocity field was characterised by PIV whereas in open jet test section only polars were recorded. These data should bring some insight onto the effect of a modification of farfield boundary conditions. All the experimental results are provided into numerical data files in Appendix 3-4.

According to VFE-2 common notations NASA model is named Model 1, sharp and medium leading edge ONERA models are respectively named Model 4 and Model 5.

20.3 EXPERIMENTAL SET UP

20.3.1 L1 Wind Tunnel

The tests were conducted in ONERA Lille L1 wind tunnel. The facility is a closed circuit wind tunnel working in the incompressible domain. The test section is axisymmetrical 2.40 m in diameter and 2.40 m long. Walls are movable so that it is possible to operate in solid walls or in open jet tunnel. The maximum freestream velocity is 75 m/s in solid walls and 60m/s in open jet test section. The turbulence rate is 1.3%. No wall corrections were applied.

20.3.2 Model 1

The NASA model is a 65° swept symmetrical flat plate delta wing, c_r = 0.49023 m in root chord. It can be equipped with four interchangeable leading edges. Surfaces are represented by a fully analytical function. The different leading edges are named 'sharp', 'small', 'medium' and 'large' and are defined by their respective curvature radius $r/\bar{c}$ = 0, 0.05, 0.15 and 0.30. As previously mentioned only 'sharp' and 'medium' leading edges are considered here. The model is provided with static pressure ports located on the lower surface and on the upper surface at ξ = 0.2, 0.4, 0.6, 0.8 and 0.95. In addition, orifices were located on both the port and the starboard 'medium' leading edges. A more detailed description of the model is given in [20-5] and [20-6]. A sketch of the model and a view in the test section are provided in Figure 20-1.

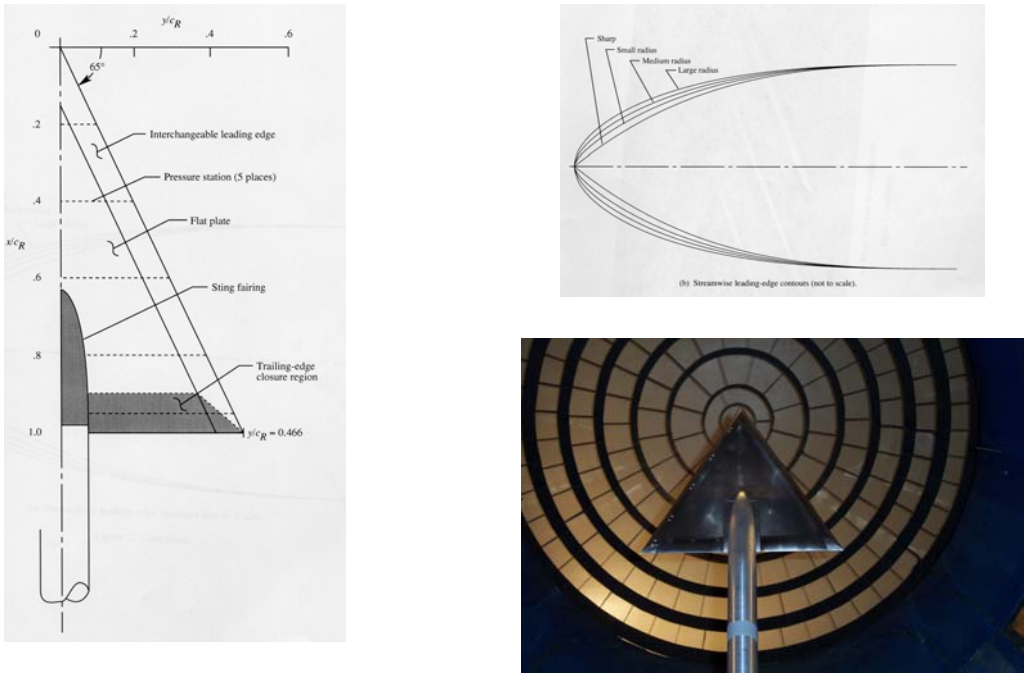

Figure 20-1: Sketches of Model 1 (from [20-5]) and View in Test Section.

20.3.3 Models 4 and 5

In order to perform forces and moments measurements under acceptable uncoupling conditions two resin one-piece copies of the 'sharp' and 'medium' NASA models were manufactured. The equipment of these models was reduced as far as possible. Every model was provided with 10 pressure taps located such that comparisons with LTPT data could be possible (Figure 20-2).Two accelerometers allowed the incidence measurements to be checked. A geometrical control of both shapes and pressure ports location has been made on NASA and ONERA models. Shapes were measured along three chord stations situated at Δx = 98.23 mm, 196.23 mm and 392.23 mm from the apex. Results have been compared to the analytical functions and are reported on Table 20-1. It can be observed that discrepancies are of same order when comparing Model 1 and Model 5 with the theoretical shapes. But Model 4 variations are twice Model 1 ones. These differences can be attributed to the fact that Model 4 and 5 are made out of resin. Their amplitudes however remain bounded within acceptable limits. Pressure ports locations are reported in Table 20-2. Discrepancy is higher for Model 4 and 5, but if the extreme cases are eliminated, differences are of same order than Model 1 ones.

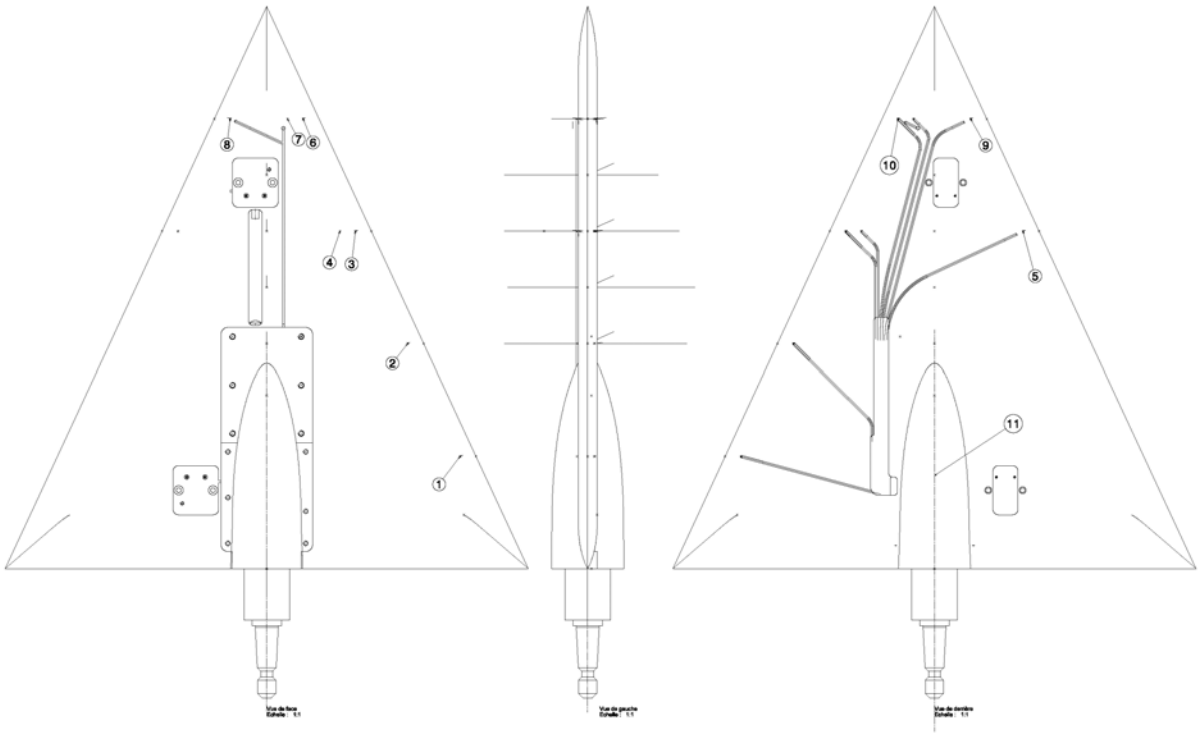

Figure 20-2: Sketch of Model 4 and 5 with Pressure Ports Locations.

Table 20-1: Geometrical Discrepancy along Three Chord Sections between Each Model and the Analytical Shape: Maximum Variations in mm

Chord Section		Model 1 Sharp	Model 1 Medium	Model 4	Model 5
x = 98.23 mm	Δz max(+)	0.147	0.162	0.278	0.245
	Δz min(-)	0.147	0.123	0.234	0.235
x = 196.23 mm	Δz max(+)	0.181	0.234	0.278	0.143
	Δz min(-)	0.204	0.157	0.22	0.125
x = 392.23 mm	Δz max(+)	0.112	0.206	0.217	0.216
	Δz min(-)	0.096	0.186	0.181	0.142

Table 20-2: Geometrical Discrepancy of Pressure Port Locations Reduced by the Diameter d = 0.3 mm of the Orifice

	Model 1 Sharp	Model 1 Medium	Model 4	Model 5
Theoretical Location (mm)	**δl/d =**	**δl/d =**	**δl/d =**	**δl/d =**
x = 98.04; y = 32.00 (lower s.)			1.7013	2.3393
x = 98.04; y = -32.00 (lower s.)	0.4028	0.7951	1.6826	3.1525
x = 98.04; y = -32.00			1.2257	1.1324
x = 98.04; y = 18.29	0.7923	1.1823	1.7754	0.8750
x = 98.04; y = 32.00	0.3887	0.9718	1.6275	0.7775
x =196.08; y = -77.72 (lower s.)			1.4380	1.8406
x = 196.08; y = 64.01	1.1035	1.7745	1.4896	0.5000
x = 196.08; y = 77.72	0.4123	0.7063	1.1557	0.3819
x = 294.13; y = 123.43	1.0022	1.3342	0.8800	0.3801
x = 392.17; y = 169.16	0.9672	1.1126	0.5831	6.4849

20.4 RESULTS

20.4.1 Model 1 in Solid Walls Configuration

20.4.1.1 Test Section Apparatus

The NASA sting supplied with the model was too long and too heavy to be easily fitted to the L1 structure. So the model in L1 was supported by a sting rigidly locked underneath the test section with a trolley moving along a hemi circular cradle. This set up provided two degrees of freedom in rotation, allowing imparting incidence and side-slip to the model. The displacement in incidence of the trolley being limited within ±15° it was not possible to cover the entire incidence range within the same run. So a metallic arm provided with a movable part held the sting line in position, so as to cover the incidence range within two runs, from -5° to 15°, and then from 13° to 40° after taking away the movable part. The accuracy was 0±0.15° in rolling and 0±0.1° in incidence and slide-slip. The fairing was geometrically similar to the NASA fairing (Figure 20-3).

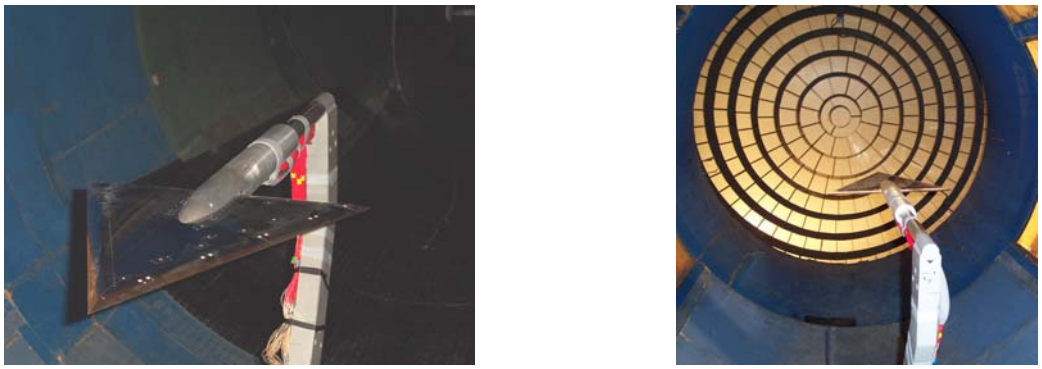

Figure 20-3: Views of the Model 1 in Test Section.

20.4.1.2 Tests

Static pressures were transmitted from the obstacle to PSI modules. A 25s time interval for propagation and 15s for stabilization had been estimated during calibration. A 60s time interval for stabilization was retained during tests. Signals were filtered at 2 Hz and averaged on 100 points before recording. The sampling rate was 10 Hz. Due to high number of pressure ports, it was not possible to record all the signals simultaneously. Therefore the different braids were successively connected to the sensors, and for a given configuration of connected pressure taps the whole incidence range was investigated before proceeding to the others braids. From three to four cablings were necessary to record all the pressures relative to each leading edge. Some blocked pressure taps were identified during the phase of numbering ports. They were kept off during the tests. Some others presenting an unusually long time for stabilization were identified but nevertheless taken into account for measurements. They deliver pressure levels very different from their neighbouring, are in that way easily recognizable and therefore have to be neglected.

20.4.1.3 Results

For each leading edge, pressure distributions at upper surface are presented in Figure 20-4 and Figure 20-5 for $5° \leq \alpha \leq 30°$ with a step of 5°, except for the 'sharp' for which LTPT data base is limited at $\alpha = 28°$. For the 'medium', surface-pressures at L1 from the inboard part of the wing at station $\xi = 0.60$ and over the entire span at station $\xi = 0.95$ exhibited a great shift when comparing with LTPT ones. These discrepancies were attributed to an offset effect and as a consequence are not reported on Figure 20-4 and Figure 20-5.

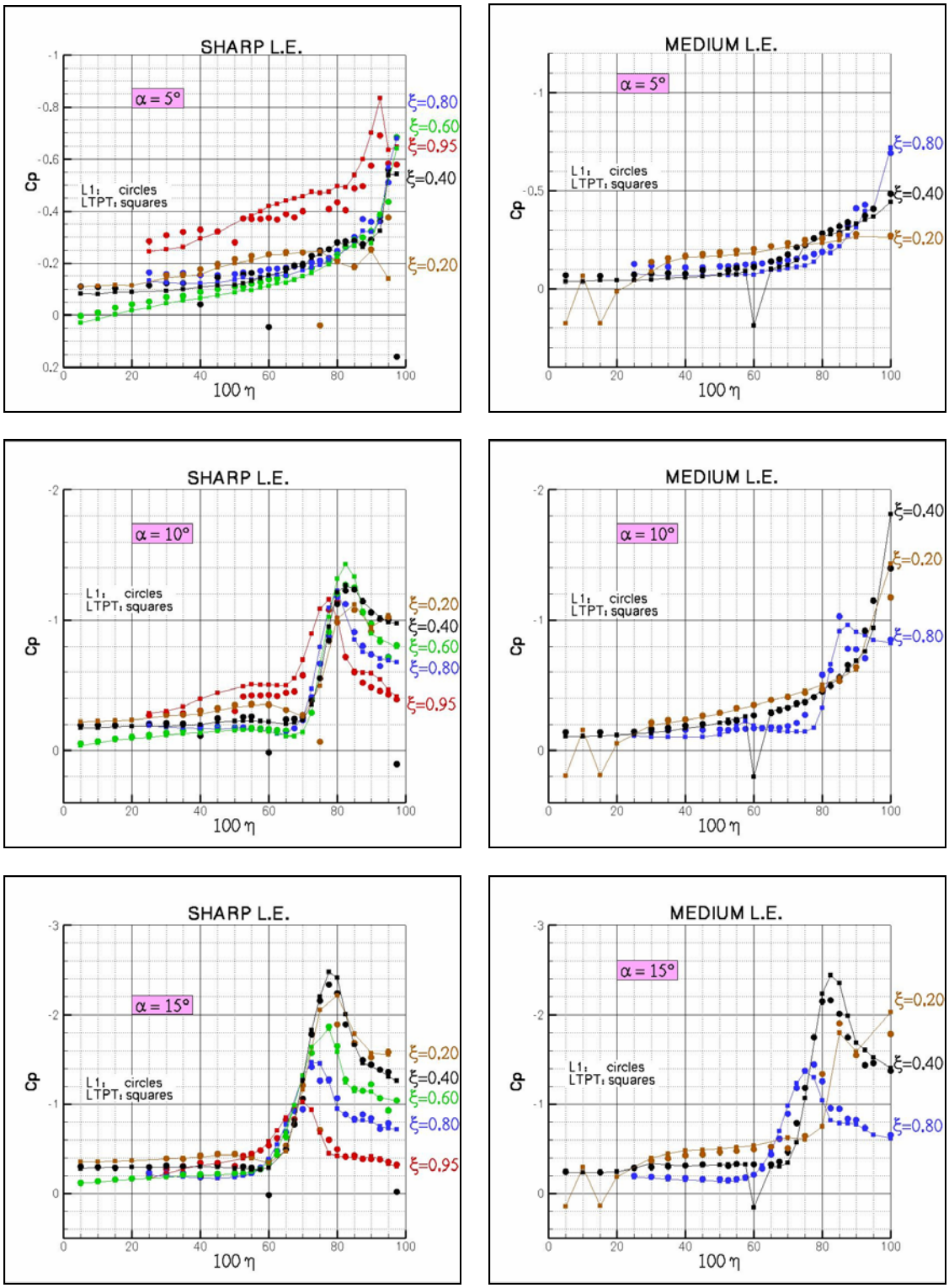

Figure 20-4: Pressure Distributions on Model 1 Upper Surface – Solid Walls (Sharp: $Re_{mac} = 10^6$ at L1; $Re_{mac} = 1.5 \times 10^6$ at LTPT – Medium: $Re_{mac} = 10^6$ at L1; $Re_{mac} = 2 \times 10^6$ at LTPT).

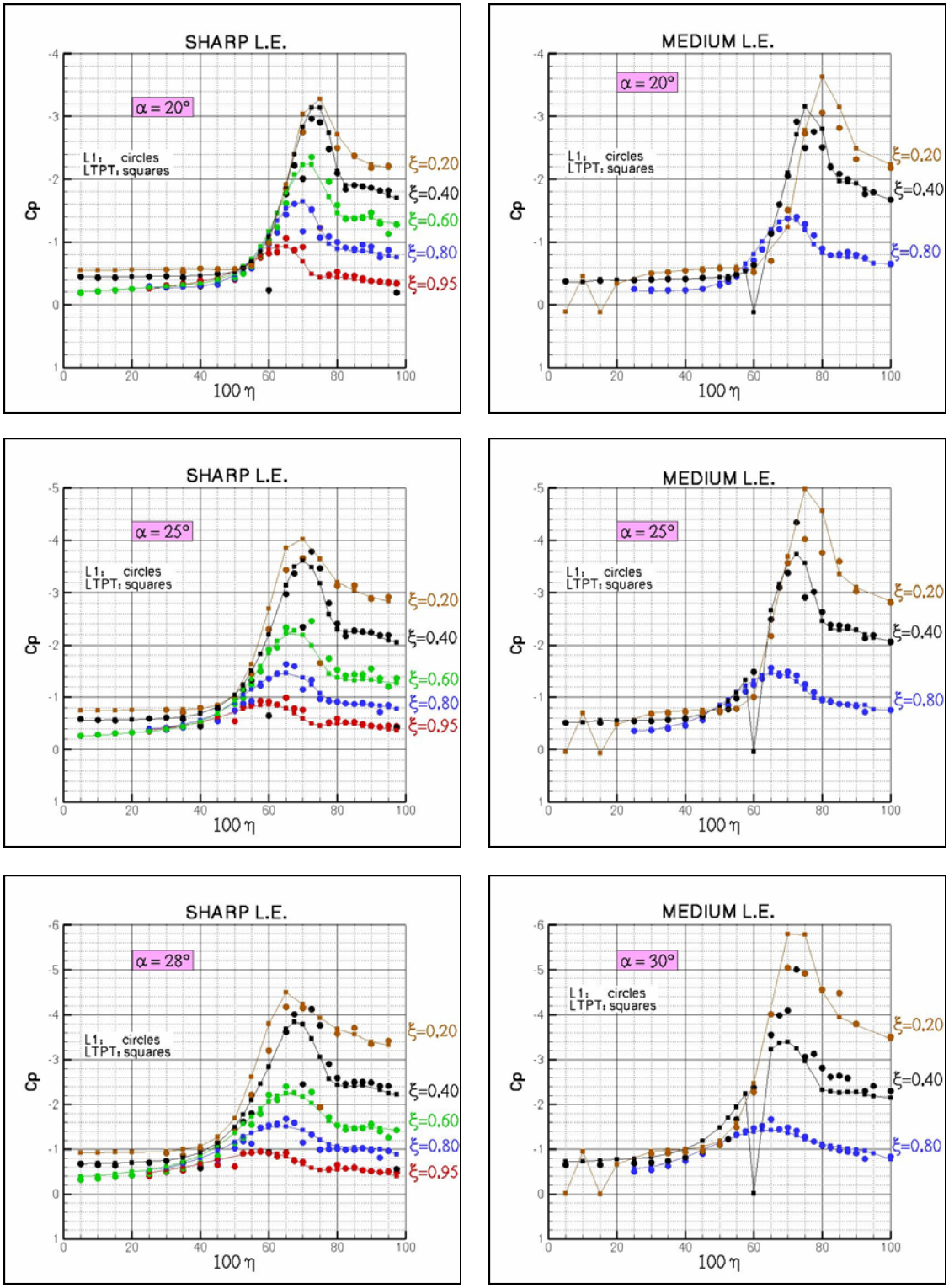

Figure 20-5: Pressure Distributions on Model 1 Upper Surface – Solid Walls (Sharp: $Re_{mac} = 10^6$ at L1; $Re_{mac} = 1.5 \times 10^6$ at LTPT – Medium: $Re_{mac} = 10^6$ at L1; $Re_{mac} = 2 \times 10^6$ at LTPT).

At $\alpha = 5°$ variations $\Delta C_p \sim 0.05$ are observed for the 'sharp', the flow over nearly all the wing being at L1 slightly accelerated compared to LTPT. These differences remain small, of order 2% to 3% of the upstream velocity, except near the leading edge where they are somewhat higher. At the same incidence variations are slightly reduced for the 'medium'.

At $\alpha = 10°$ the' sharp' leading edge produces pressure distributions in rather good agreement with LTPT ones, except that the station $\xi = 0.95$ exhibits a $\Delta C_p \approx 0.1$ more or less constant. Pressure peaks induced by the primary vortex are relatively well reproduced. For the 'medium' the pressure distributions are also very similar to the LTPT ones except at $\xi = 0.80$ where variations $\Delta C_p \approx 0.1$ are recorded on the outer part of the wing corresponding to $\eta>0.70$. It can be observed that separation did not move upstream to the apex and that the primary vortex locates downstream the station $\xi = 0.40$ both at L1 and LTPT.

At $\alpha = 15°$ the' sharp' leading edge provides results relatively similar to LTPT ones, with a suction peak slightly underestimated at $\xi = 0.20$, which could be eventually attributed to a small lateral shift of the vortex axis on upper surface. For the 'medium' results relative to the pressure peak level of the primary vortex exhibit a maximum variation $\Delta C_p \approx 0.2$ observed at $\xi = 0.40$. It is clear that the differences in Reynolds numbers between the two experiments can play a role and partly explain these discrepancies.

At $\alpha = 20°$ L1 and LTPT pressure distributions are rather similar for both leading edges. Primary vortex is correctly captured in position and amplitude. As previously observed 'medium' distributions exhibit differences a little bit more pronounced in the vortex peak, at stations $\xi = 0.20$ and 0.40.

For $\alpha \geq 25°$ the same trends are observed with variations for the 'medium' becoming more intense in the suction peak.

A good agreement is obtained between L1 and LTPT when comparing the lower surface pressure distributions. This is observed upon nearly all the wing except the station $\xi = 0.95$ where small variations decreasing with α are recorded between 5° and 25° (Figure 20-6). The gradual displacement of separation toward the apex can be deduced from an analysis of pressures transmitted from ports located along the leading edge [20-7]. Propagation of separation induces a pressure increase characterised by a bump in $C_p(\alpha)$ graph. Separation moves upstream to the apex when incidence increases (Figure 20-7). As a general rule peak pressure levels are lower at L1. Furthermore, while peaks at $\xi = 0.40$ and $\xi = 0.60$ are recorded for the same values of incidence in the two wind tunnels, a shift of about 1° incidence exists at $\xi = 0.20$, 0.80 and 0.95. Variations in these very high gradients zones could be attributed to a Reynolds number effect.

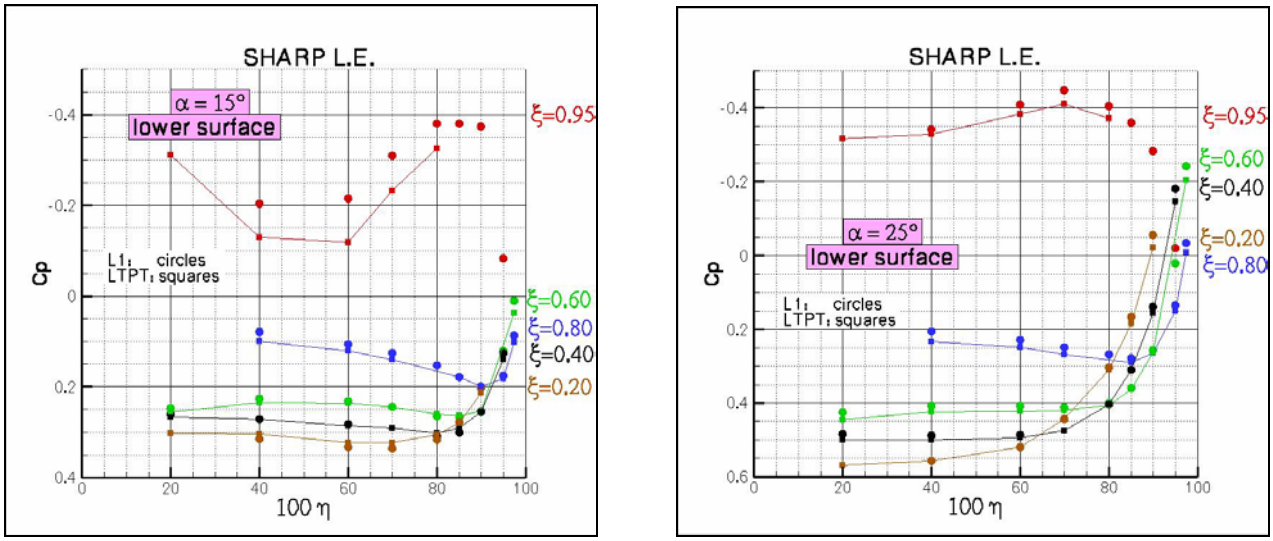

Figure 20-6: Pressure Distributions on Model 1 Lower Surface (Sharp: $Re_{mac} = 10^6$ at L1; $Re_{mac} = 1.5 \times 10^6$ at LTPT).

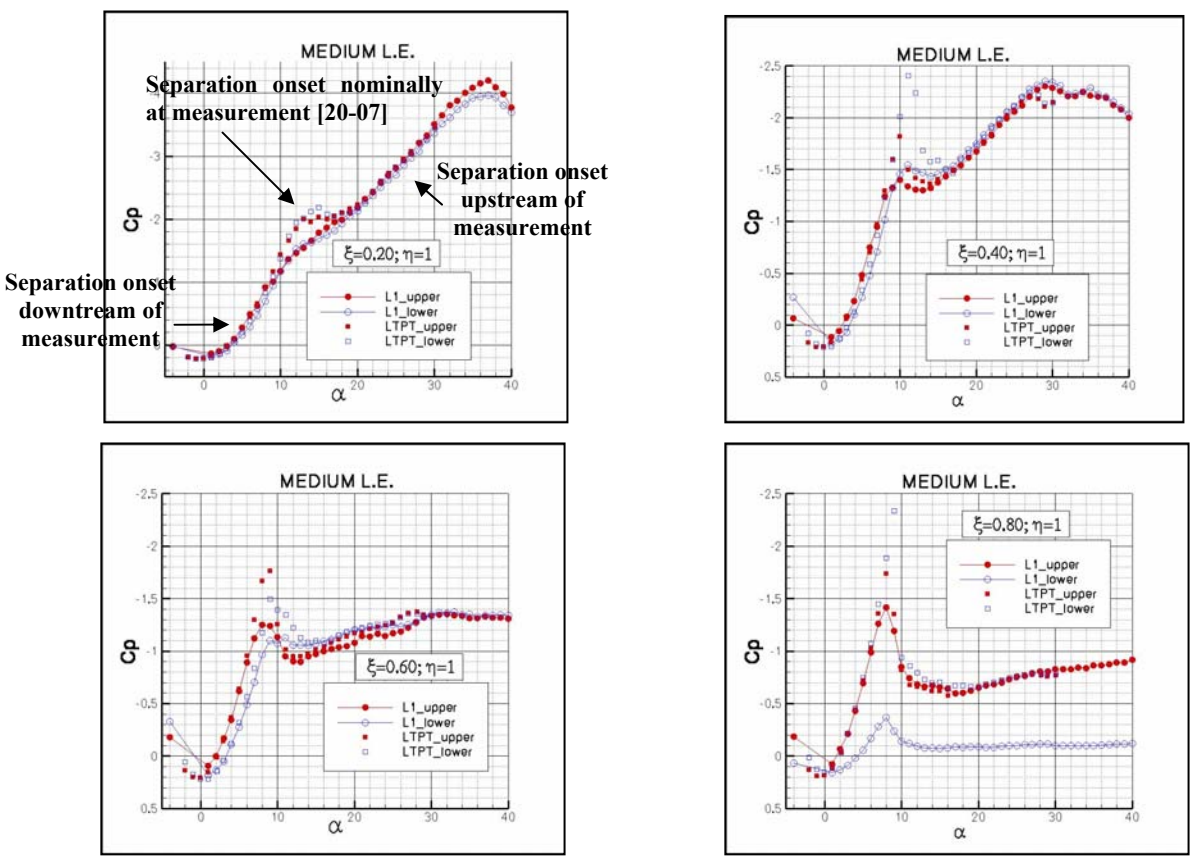

Figure 20-7: Pressure Distributions along the Model 1 Leading Edges. Correlation of separation onset with pressure distribution according to J.M. Luckring [20-7] (Medium: $Re_{mac} = 10^6$ at L1; $Re_{mac} = 2 \times 10^6$ at LTPT).

20.4.2 Forces Measurement in Open Jet Tunnel (Model 4 and 5)

These tests can be seen as an attempt to estimate the influence of variations of the boundary conditions. An analysis of that influence on torque is made in the following paragraph, where results are compared with those obtained in solid walls. Tests were carried out with Model 4 and 5. Models were held by a specific carbon sting (Figure 20-8). The Reynolds number was $Re_{mac} = 10^6$ and incidence range $0° \leq \alpha \leq 35°$. Polars were recorded while incidence was continuously increasing at 1°/s, 2°/s or 3°/s. These measurements were then compared for validation to those recorded when the obstacle was held fixed in position, for some points between 0° and 30°.

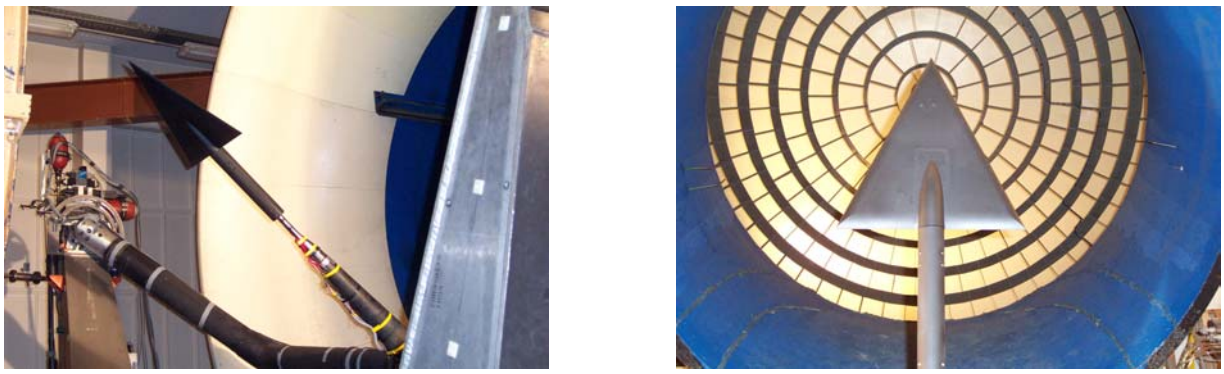

Figure 20-8: Views of Model 4 and 5 in the Open Jet Tunnel.

The wind tunnel upwash and sidewash were estimated by turning the model round the ξ-axis. In that way, two tests at $\phi = 0°$ and $\phi = 180°$ allowed to assess the upwash from lift analysis. Similar tests at $\phi = -90°$ and $\phi = +90°$ allowed to assess the sidewash. Figure 20-9 shows that there was no upwash. However a slight dissymmetry on the yaw moment increasing with incidence reveals the existence of a negative side-slip. When the wing is adjusted at $\phi = \pm 90°$ a symmetrical lateral force is recorded with a positive lift if $\phi = +90°$, which corroborates the previous side-slip (Figure 20-10).Using the value $dC_L/d\alpha = 0.0425$ deduced from the lift curve of the 'sharp' leading edge for instance, and considering that amplitude of lift at $\phi = \pm 90°$ is about 0.01 for $\alpha = 20°$, it can be estimated that the side-slip is about -0.2° at $\alpha = 20°$.

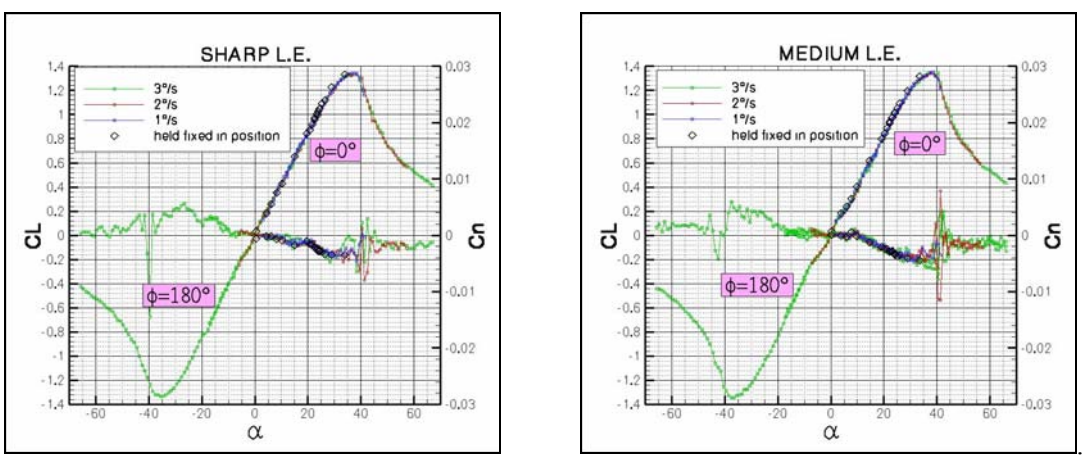

Figure 20-9: Lift and Yaw Moment Coefficients in Open Tunnel (Model 4 and 5).

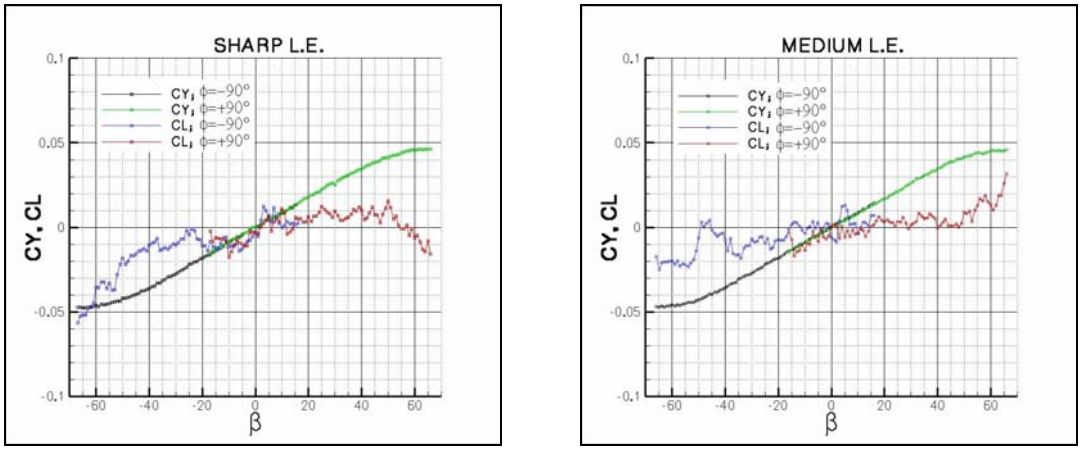

Figure 20-10: Lift and Lateral Force Coefficients in Open Jet Tunnel when the Wing Undergoes ϕ = ±90° Rotations (Model 4 and 5).

A good agreement is obtained between results relative to the different rates of incidence sweep on the one hand, and those recorded for fixed positions on the other hand (Figure 20-9 and Figure 20-11). Lift and drag curves are symmetric, at least up to stall. Lift is zero at $\alpha = 0°$ as expected and shows a good linearity on the range $0° \leq \alpha \leq 30°$ with $dC_L/d\alpha \approx 0.042$. $C_L$max is reached for $\alpha \approx 39°$ and is close to 1.35. Forces in the balance reference frame are commented in the next paragraph where they are compared with results obtained in solid walls.

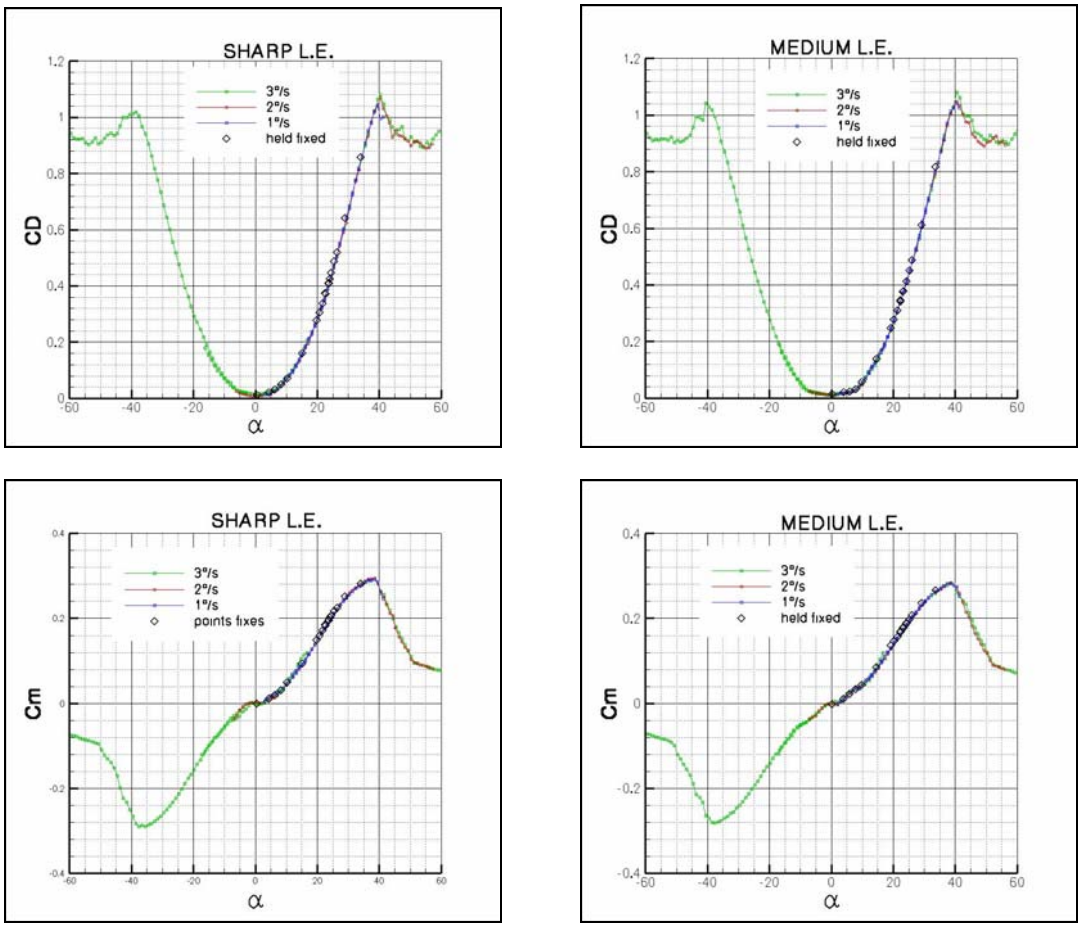

Figure 20-11: Drag and Pitching Moment Coefficients in Open Jet Tunnel (Model 4 and 5).

20.4.3 Forces Measurement and PIV Velocimetry in Solid Walls (Model 4 and 5)

20.4.3.1 Forces and Static Pressures

Normal force C_N, axial force C_A and pitching moment C_m coefficients measured at L1 are presented for each leading edge in Figure 20-12 and are compared with the values recorded in open jet test section. Differences between the two test sections are very weak for C_N and C_m. They become more intense on C_A when $\alpha>10°$. Apparently there is no explanation for that discrepancy on C_A. As expected, axial force amplitude is higher for the medium as suction effect from the leading edge is promoted.

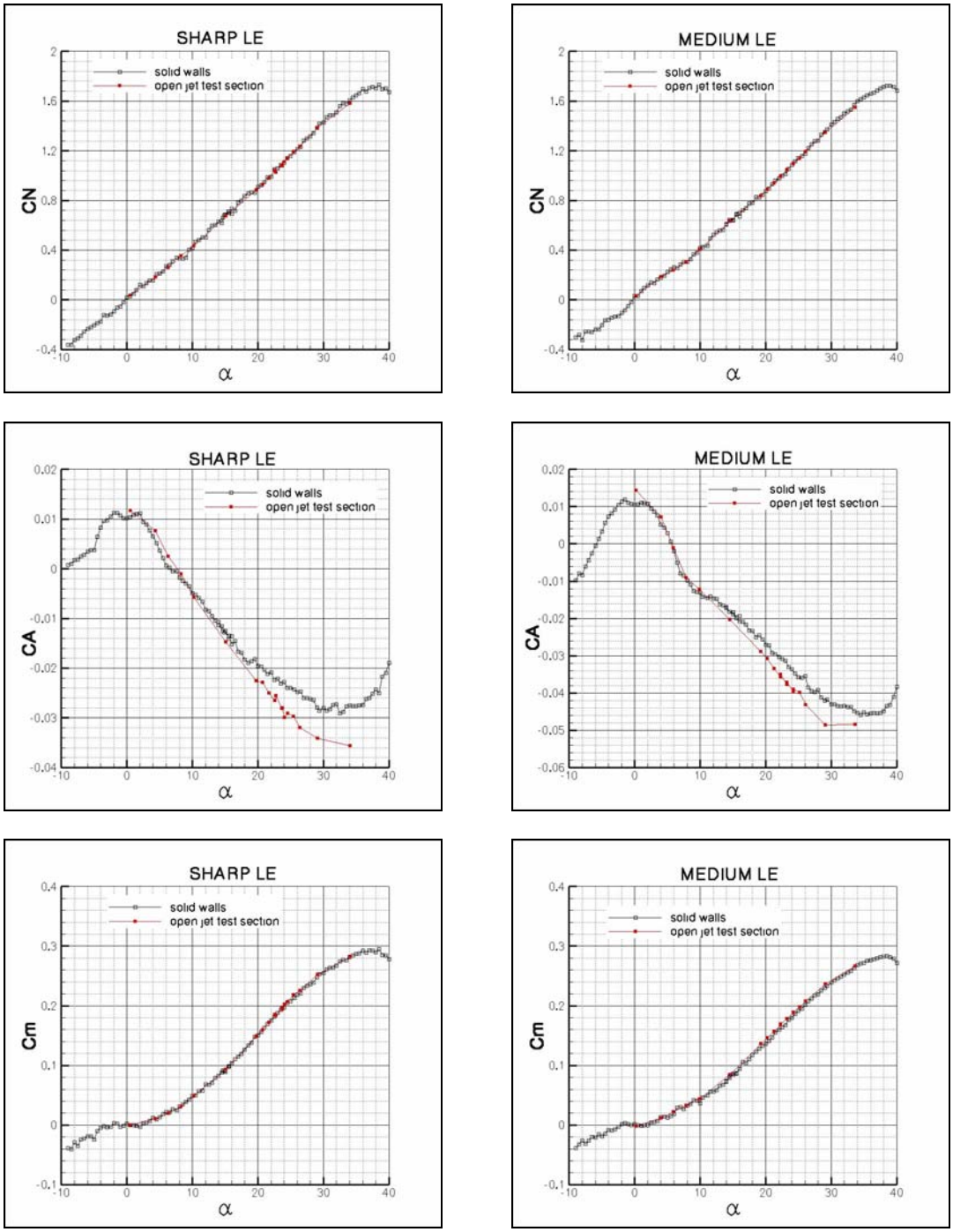

Figure 20-12: Normal Force, Axial Force and Pitching Moment Coefficients at L1 (Model 4 and 5).

Comparison of static pressures on the obstacle with LTPT distributions exhibits some differences (Figure 20-13). Variations are similar in amplitude to those recorded in open jet tunnel, although slightly smaller for the open jet tunnel. These pressure distributions are recapitulated in a more explicit form on Figure 20-14 and Figure 20-15

where it is possible to compare pressure distributions from the same model for both test section configurations at L1 (Model 4 and 5), pressure distributions in solid walls at L1 and LTPT from the same model (Model 1), pressure distributions in solid walls at L1 from different models (Model 1, 4 and 5).

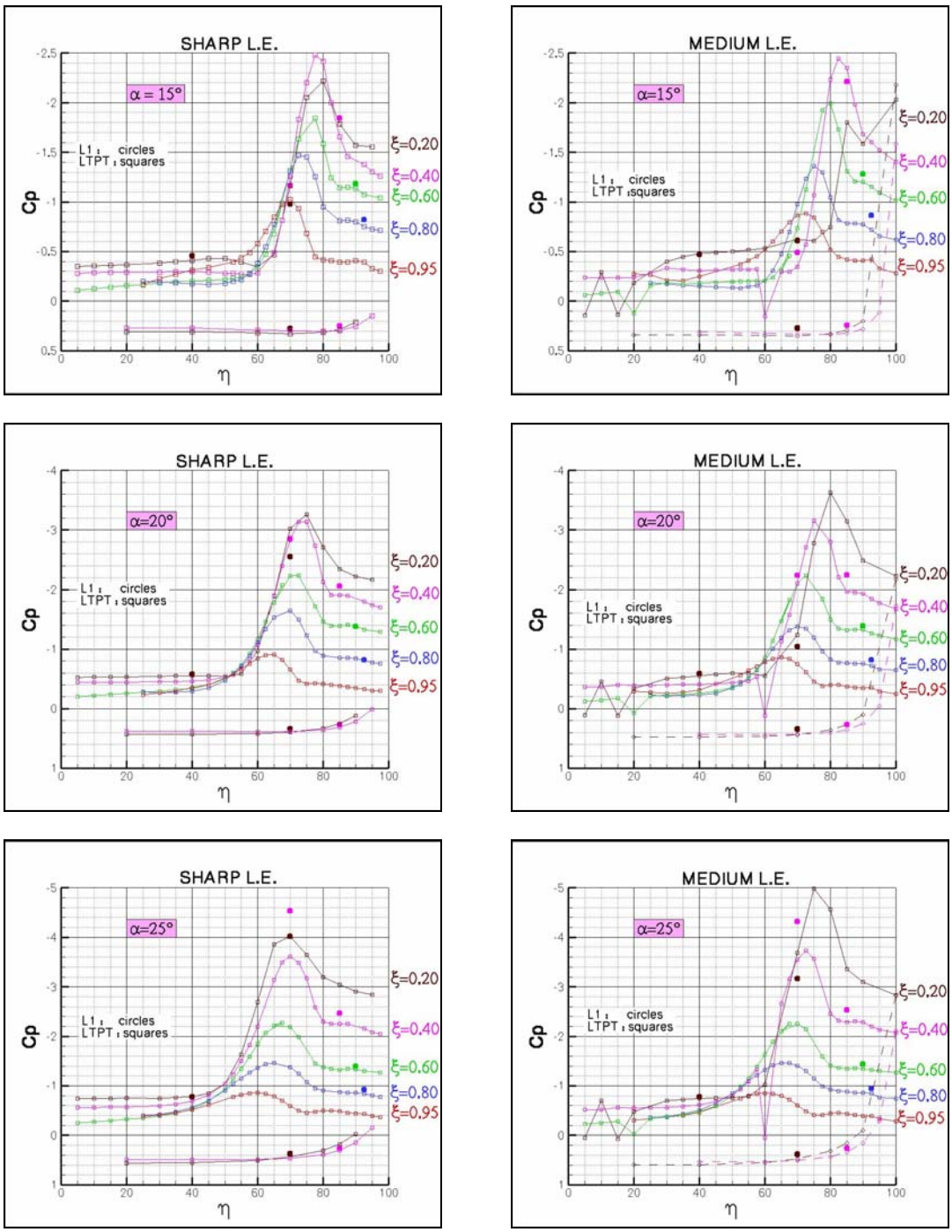

Figure 20-13: Pressure Distribution at L1 in Solid Walls (Model 4 and 5) and Comparison with LTPT (Sharp: $Re_{mac} = 10^6$ at L1; $Re_{mac} = 1.5 \times 10^6$ at LTPT – Medium: $Re_{mac} = 10^6$ at L1; $Re_{mac} = 2 \times 10^6$ at LTPT).

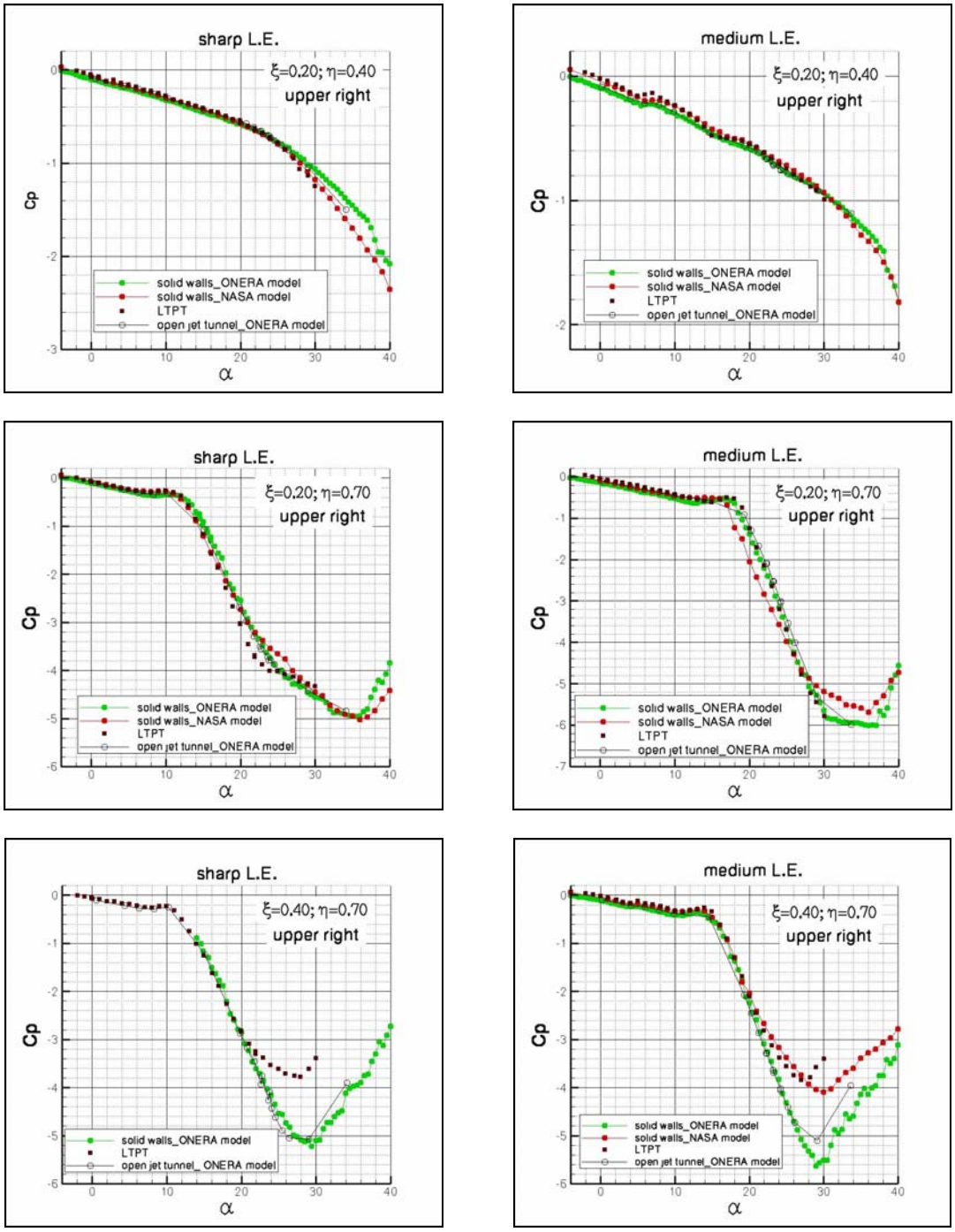

Figure 20-14: Comparison of Pressure Coefficients Measured in Solid Walls and in Open Jet Tunnel (Upper Surface, h ≤ 0.70).

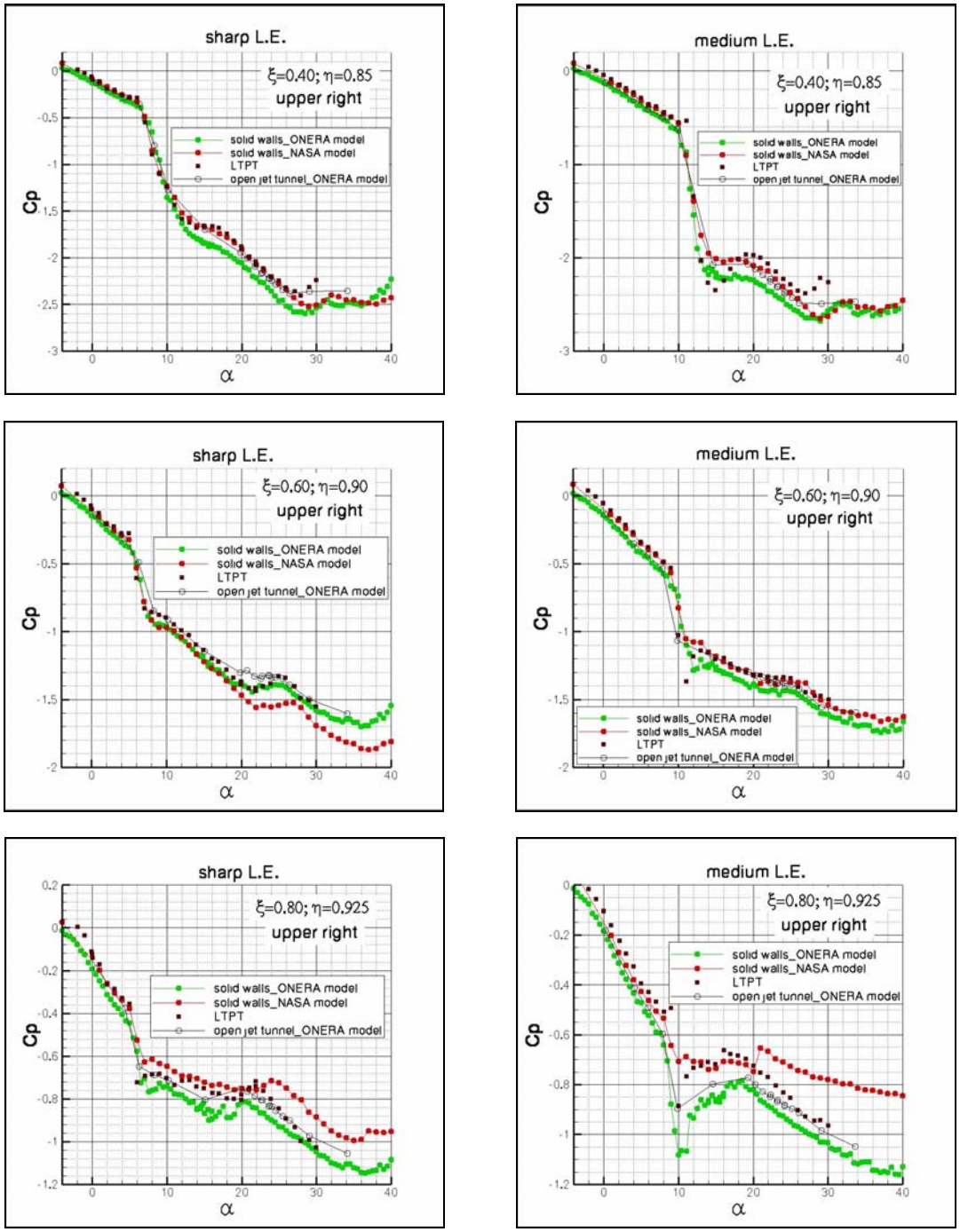

Figure 20-15: Comparison of Pressure Coefficients Measured in Solid Walls and in Open Jet Tunnel (Upper Surface, h > 0.70).

Considering the differences in Reynolds numbers, the agreement between L1 and LTPT pressures at Model 1 upper surface can be estimated as acceptable over practically the whole incidence range if $\xi \leq 0.60$ (Figure 20-14,

Figure 20-15). At station $\xi = 0.80$ the variation increases when $\alpha>20°$ and $\eta\geq0.90$, corresponding to the area of the secondary vortex influence. Pressures at lower surface are similar (Figure 20-16).

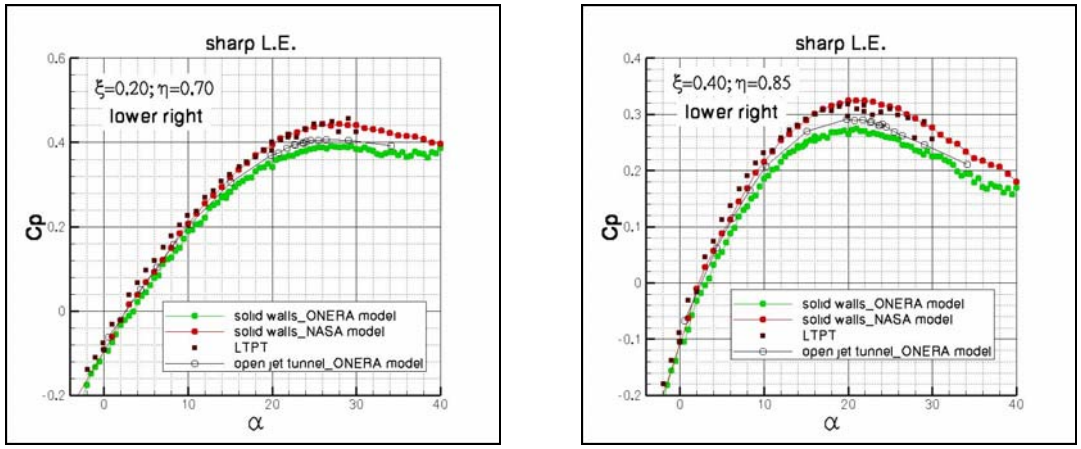

Figure 20-16: Comparison of Pressure Coefficients Measured in Solid Walls and in Open Jet Tunnel (Lower Surface).

If only results relative to Model 4 and 5 in solid walls and in open jet tunnel are compared, agreement on upper surface is very good over the whole incidence range for the inboard part of the wing and for the region wetted by the primary vortex (more or less for $\eta<0.80$). On the other hand, for the outboard part of the wing ($\eta>0.80$) a small variation exists when $\alpha>10°$ approximately, linked to the upstream motion of separation towards the apex and then to the secondary vortex development. The pressure is weaker in solid walls, which seems normal due to the confined aspect of the test section (Figure 20-14, Figure 20-15). Pressure distributions at lower surface are somewhat different (Figure 20-16). As a conclusion, the influence of test section configurations affects only the vicinity of the leading edge, where phenomena take place in connection with the upstream moving of separation towards the apex and then with the secondary vortex development if incidence increases more. Curiously results from the open jet tunnel test section are more similar to LTPT ones than results in solid walls are.

When the results obtained in solid walls at L1 with Model 1 and Model 4 and 5 are compared, no significant variations should be logically observed as models are identical according to the geometrical control (§20.2.3). However it appears that the pressure distributions from Model 1 at L1 are rather in better agreement with LTPT ones than those from Model 4 and 5 are (Figure 20-14, Figure 20-15). Over the inboard part of the wing flows are closely similar (Figure 20-14). On the other hand, at primary vortex location ($\xi = 0.40$, $\eta = 0.70$) the pressure peak amplitude is much more intense for Model 4 and 5. Furthermore, on the outer part of the wing, the pressure distributions from Model 4 and 5 are generally lower than those recorded in solid walls with the Model 1, which would indicate that the upstream moving of separation and then the development of the secondary vortex occur probably sooner with Model 4 and 5 (Figure 20-14, Figure 20-15). Only the small variations between the models geometries can explain these discrepancies.

20.4.3.2 Analysis of Axial Force Correlation with the Flow Structure

Figure 20-17 compares C_A evolutions in solid walls between 'sharp' and 'medium' leading edges. For $\alpha>6°$ it can be observed that the suction effect induced at leading edge promotes an axial force which amplitude is more intense for the 'medium' than for the 'sharp'. Probably these differences can be related to the primary

vortex development which occurs differently according to the bluntness of the leading edge. For the 'medium' leading edge case the primary vortex development can be correlated to the gradual progression of separation towards the apex when α increases. Analysis of pressures transmitted from ports situated along the leading edge provides a means to locate the separation onset and its displacement when incidence is varying [20-7]. Figure 20-7 reproduces J.M. Luckring's analysis on LTPT data [20-7] and makes a comparison with measurements recorded at L1 with the same model. There are some differences between the results partly due to the fact that the Re_{mac} values are not strictly identical. Indeed an increase of the Reynolds number is known to delay separation on the leading edge [20-7]. In particular it can be observed on Figure 20-7 that separation is located at $\xi = 0.20$ when $12° < \alpha < 13°$ at L1, against $14° < \alpha < 15°$ at LTPT. The same result is obtained when analysing the primary vortex footprint on upper surface pressures (Figure 20-18). Now at L1 it is precisely for $\alpha \sim 12°$, that is to say when separation is moved upstream to the apex and when the origin of the primary vortex coincides with the apex, that the 'medium' $C_A(\alpha)$ curve slope changes indicating a decrease of the suction effect (Figure 20-17). A similar analysis can be conducted for the 'sharp' although this leading edge is not equipped with pressure ports. Indeed it can be seen that the primary vortex suction peak has moved upstream to the apex when $\alpha = 6°$ (Figure 20-19). Because of the existence of a geometrical discontinuity at the leading edge, it can be inferred that a reattachment occurs on the 'sharp' upper surface just downstream of the leading edge when $\alpha \leq 5°$. Now it is also for $\alpha \approx 6°$ that 'sharp' $C_A(\alpha)$ curve slope changes indicating a decrease of the suction rate (Figure 20-17).These phenomena show that the influence of the primary vortex on axial force is directly related to extension and location along the leading edge of the separation line that generated the vortex. Sketches in Figure 20-20 show the influence on suction of the flow structure at leading edge. As at low incidences the flow around 'sharp' and 'medium' can be considered as attached, the suction rate keeps the same value for the 2 leading edges when $\alpha<6°$ is varying (Figure 20-17). For $\alpha>6°$ the flow around the 'sharp' leading edge is entirely separated. Because it remains then fixed, the separation line sets limits to the suction effect at upper surface and that explains why the suction rate decreases when comparing with $\alpha<6°$ case.

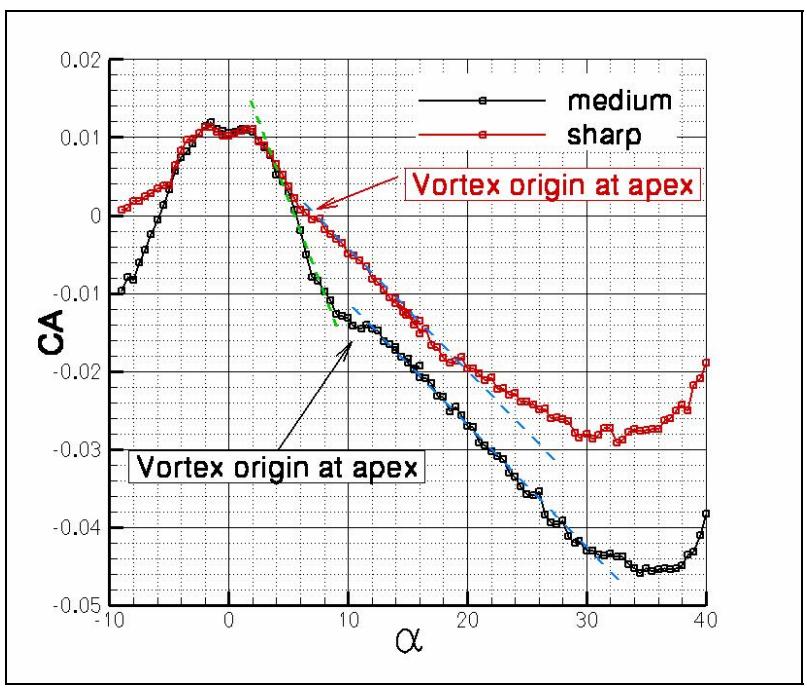

Figure 20-17: Axial Force Variations: L1, Solid Walls, $Re_{mac} = 10^6$.

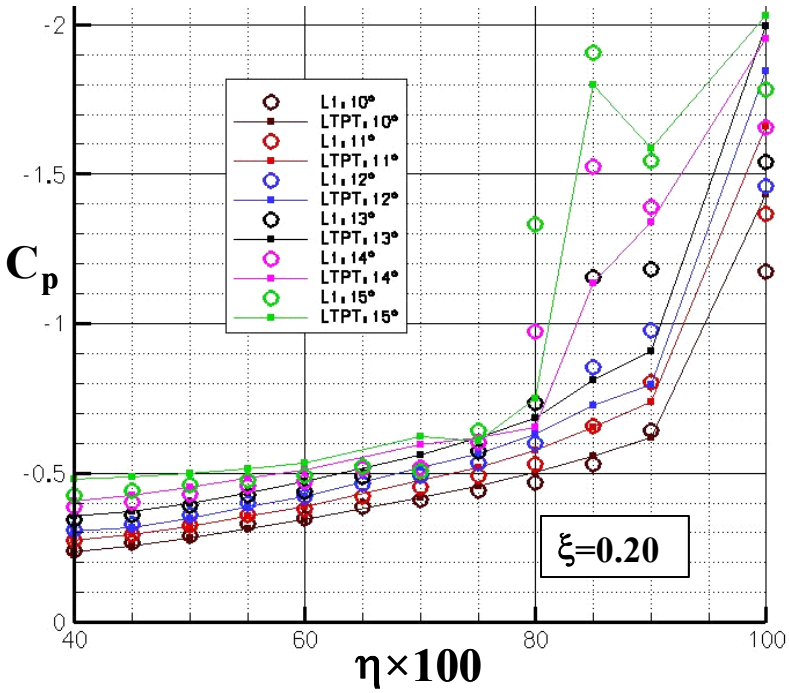

Figure 20-18: Correlation of Primary Vortex Onset at ξ = 0.20 with Medium Leading Edge Upper Surface Pressure Distribution – Model 1 – L1: $Re_{mac} = 10^6$; LTPT: $Re_{mac} = 2 \times 10^6$.

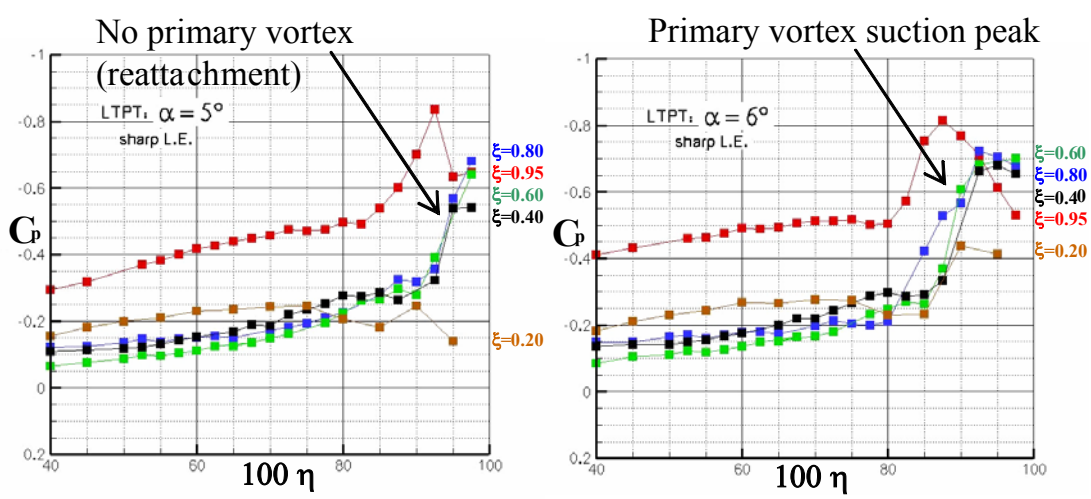

Figure 20-19: Correlation of Primary Vortex Onset with Sharp Leading Edge Upper Surface Pressure Distribution – Model 1 – LTPT: $Re_{mac} = 1.5 \times 10^6$ (Chu and Luckring [20-5]).

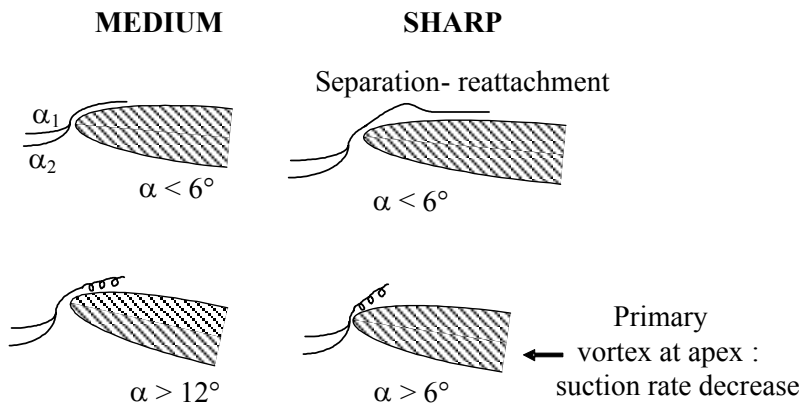

Figure 20-20: Influence of the Leading Edge Flow Structure on Suction Rate.

So, the suction effect for the 'sharp' is growing if $\alpha>6°$ is increasing but the growing is then only due to suction variations at the lower surface. The same phenomenon can be observed for the 'medium' leading edge when $\alpha\geq12$ °, so it is not surprising that the suction rate is equal to the 'sharp' one over that range of incidence (Figure 20-17). But as the separation line is now located slightly downstream at the upper surface, the contribution of the upper surface to suction is stronger than for the 'sharp', leading to a shift between the two parallel lines characterising $C_A(\alpha)$ variations when vortex origin is at apex (Figure 20-17). That behaviour is observed at $Re_{mac} = 10^6$.

20.4.3.3 Flow Field Velocity Measurements by PIV

Velocity fields were measured by stereoscopic PIV across plans located at stations ξ = 0.30, 0.40, 0.50, 0.60, 0.70. The objective was to record velocity maps when the vortex breakdown point was located approximately at mid-chord. According to discussions within the AVT-113 task group this should correspond to $23°\leq\alpha\leq25°$. So incidence of the test was fixed at 24.7°. In addition to measurements in plans normal to the wing chord, velocity measurements were performed by 2C-PIV in a plan parallel to the obstacle and 4mm far from the wing (Figure 20-21, Figure 20-22). The laser sheet was 1 mm thick.

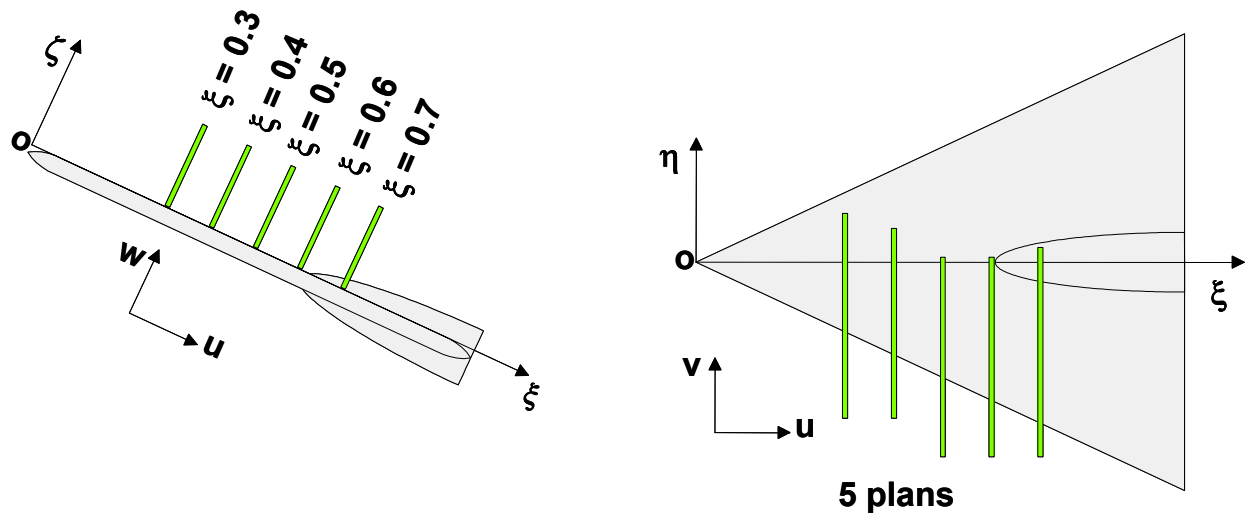

Figure 20-21: Localization of Stereoscopic PIV Plans.

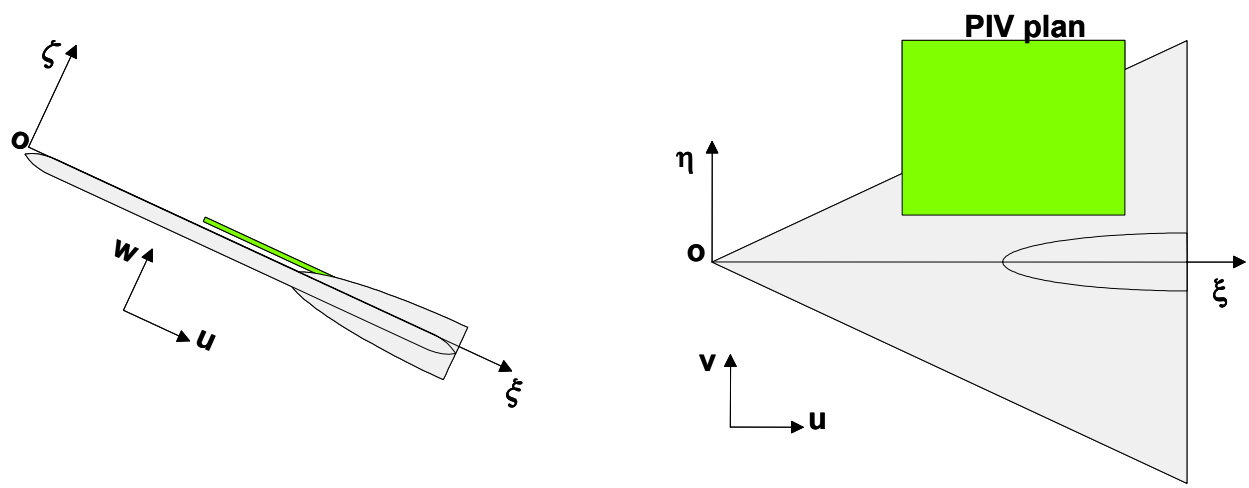

Figure 20-22: Localization of the PIV Plan Parallel to the Wing.

Figure 20-23 and Figure 20-24 provide some examples of vorticity and longitudinal velocity fields related to 'sharp' and 'medium' leading edges. Decreasing of the vortex intensity is clearly observed when moving downstream. Vortex intensity of the 'medium' leading edge is weaker than the 'sharp' one, but in both cases vortex breakdown occurs downstream the station $\xi = 0.70$, the longitudinal velocity at $\xi = 0.70$ being still highly positive. Such results were not expected a priori. In particular they do not seem in good agreement with University of Munich ones for which the vortex breakdown point is located, for open jet tunnel conditions and $Re_{mac} = 10^6$, at $\xi = 0.50$ when $\alpha = 23°$ [20-8].

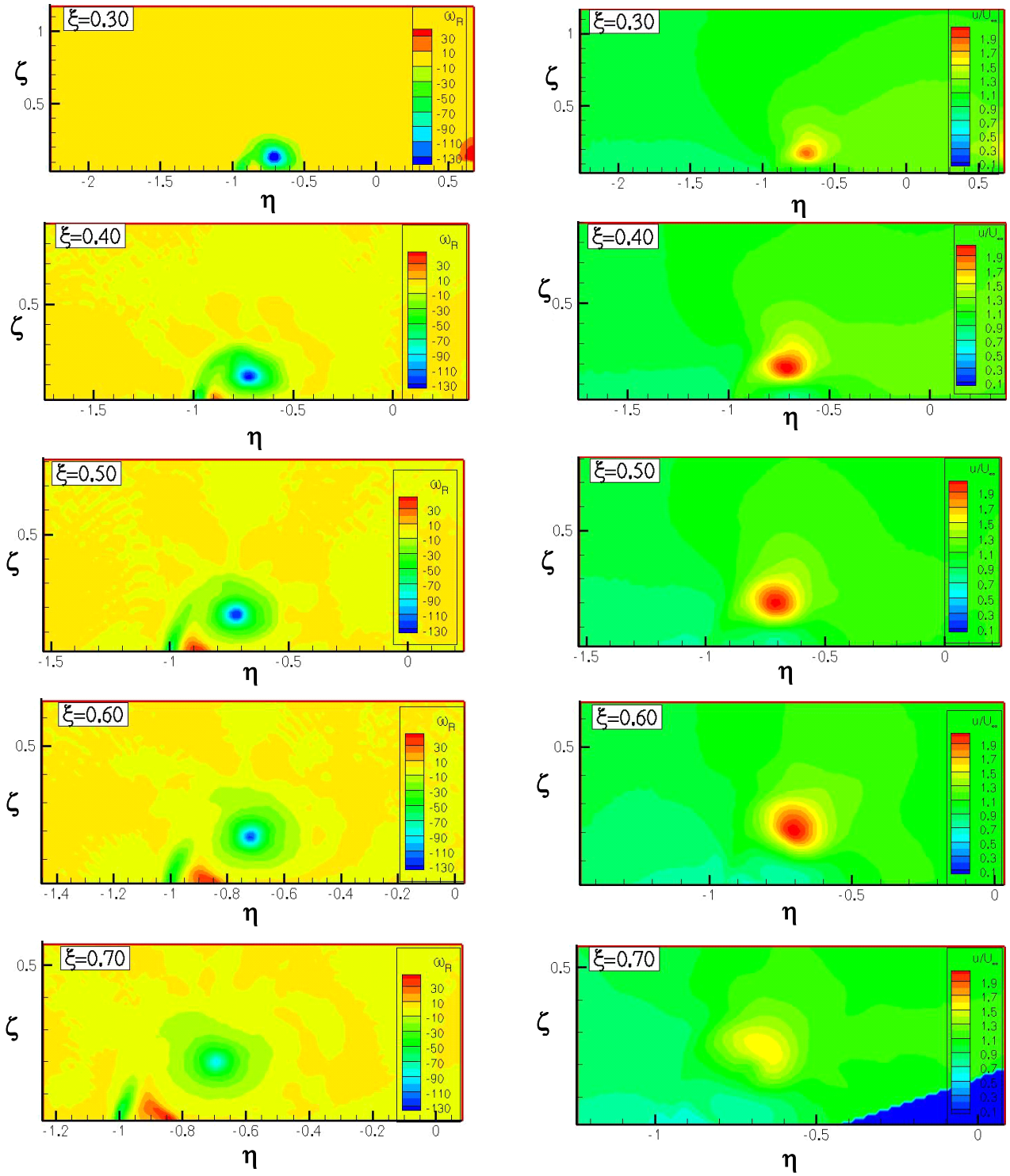

Figure 20-23: Vorticity and Longitudinal Velocity Fields – Model 4 – α = 24.7° – L1: $Re_{mac} = 10^6$, M = 0.133.

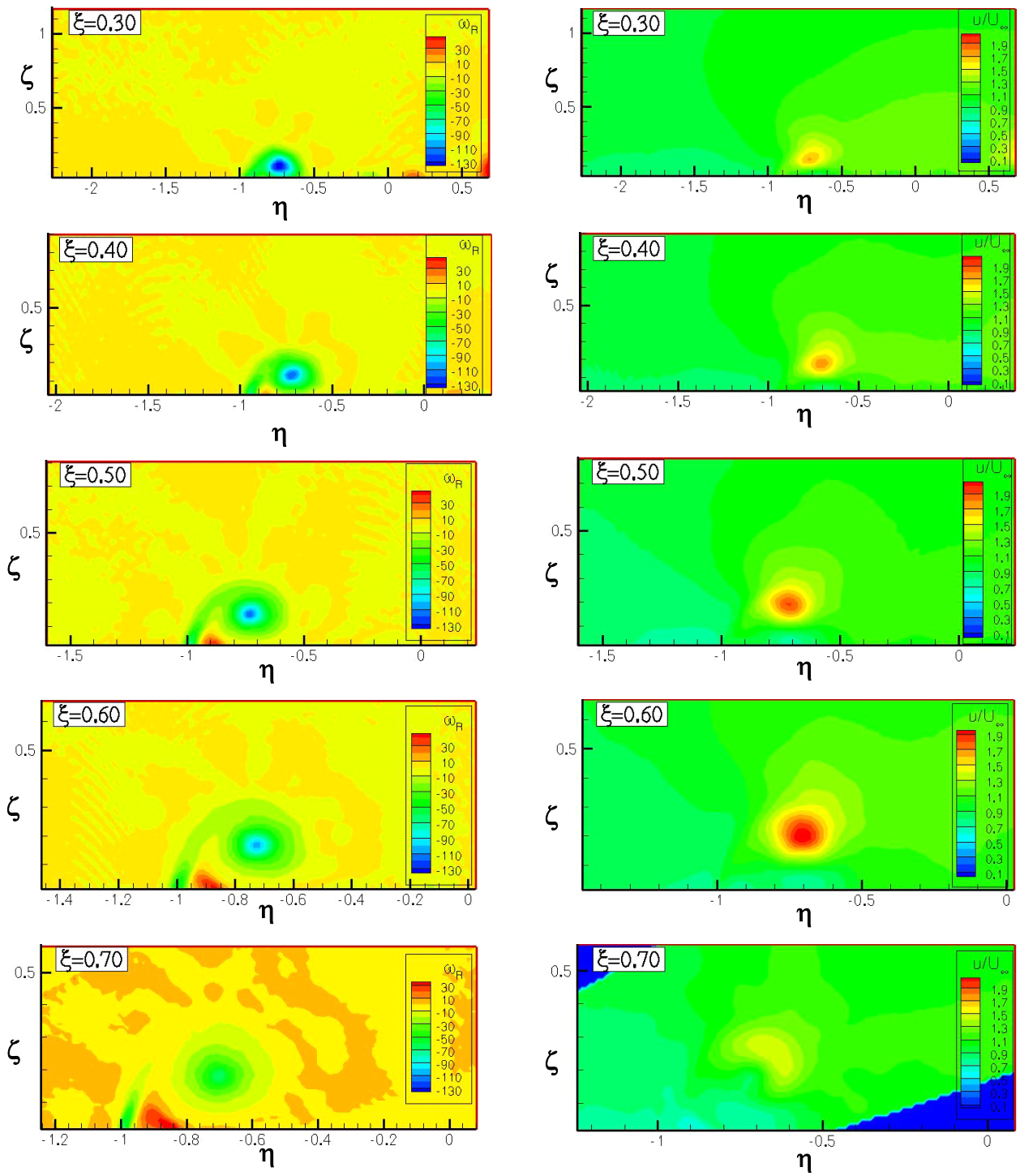

Figure 20-24: Vorticity and Longitudinal Velocity Fields – Model 5 – α = 24.7° – L1: $Re_{mac} = 10^6$, M = 0.133.

Figure 20-25 exhibits vorticity and velocity fields measured by PIV 2 components in a plan parallel to the wing. A comparison with Figure 20-23 and Figure 20-24 lead to primary and secondary vortex identification. For ξ>0.80 a low speed area within the secondary vortex probably reveals the breakdown of that structure, while primary vortex obviously is not yet breakdown.

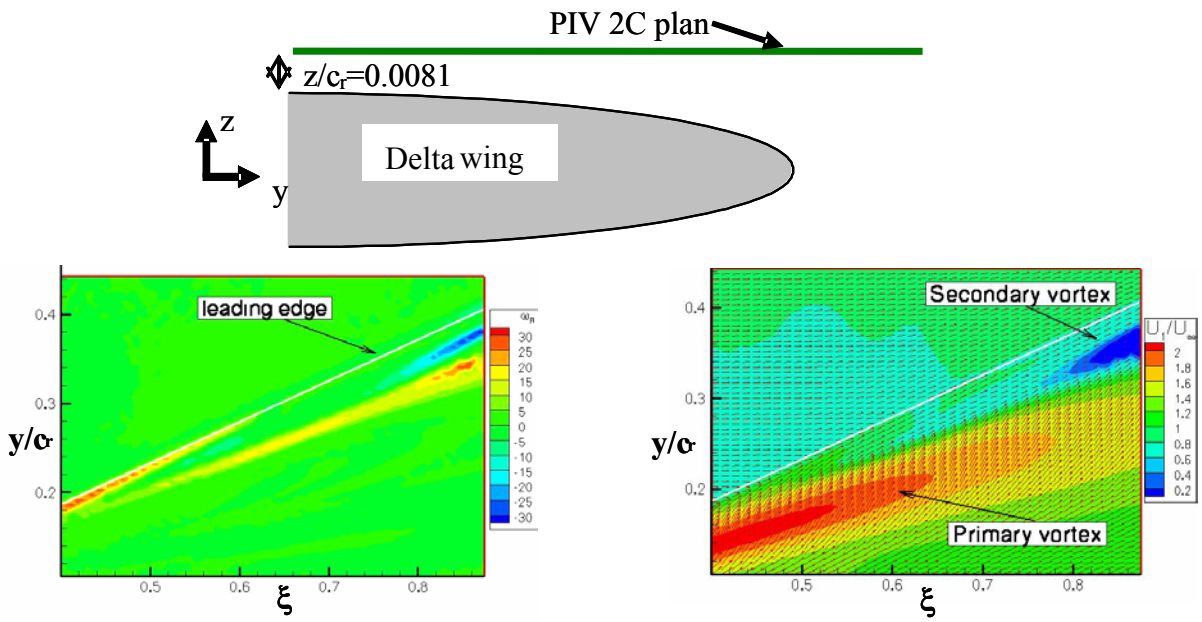

Figure 20-25: PIV 2C Vorticity and Velocity Fields in a Plan Parallel to Upper Surface – α = 24.7° – Model 5 – L1: $Re_{mac} = 10^6$, M = 0.133.

20.5 CONCLUSIONS

This work allowed to complete available data bases by measuring aerodynamic forces over a large range of incidence at low Reynolds and Mach numbers. Normal force and pitching moment are in good agreement with corresponding data from LTPT and NTF. The axial force depends on the suction effect and consequently on the flow structure at leading edge. So it appears to be directly correlated with the progressive upstream extension of separation along the leading edge when incidence is increasing. Surface pressures at L1 and LTPT are globally in good agreement but exhibit some variations partly due to differences in Reynolds numbers. Because the separation line is fixed at leading edge, 'sharp' is less affected by these variations. Especially at high incidence and in the vicinity of the leading edge, surface pressures seem somewhat affected by the models used as well as by the test section configuration. So impact of these parameters has not to be neglected. Velocity fields by PIV show that the vortex breakdown occurs at L1 for α>25°. That value is a little larger than initially expected.

20.6 REFERENCES

[20-1] Hummel, D.: *On the Vortex Formation Over a Slender Wing at Large Incidence*, AGARD-CP-247, Paper N° 15, January 1979.

[20-2] Rockwell, D.: *Three Dimensional Flow Structure on Delta Wings at High Angle-of-Attack: Experimental Concepts and Issues*, AIAA Paper 93-0050, January 1993.

[20-3] Delery, J.: *Aspects of Vortex Breakdown*, Progress in Aerospace Sciences, Vol. 30, No. 1, 1994, pp. 1,59.

[20-4] Visbal, M.R.: *Computational and Physical Aspects of Vortex Breakdown on Delta Wings*, AIAA Paper 95-0585, January 1995.

[20-5] Chu, J. and Luckring, J.M.: *Experimental Surface Pressure Data Obtained on 65° Delta Wing Across Reynolds Number and Mach Number Ranges*, NASA Technical Memorandum 4645, Langley Research Center. Hampton, Virginia, February 1996.

[20-6] Luckring, J.M.: *Understanding and Modeling Vortical Flows to Improve the Technology Readiness Level for Military Aircraft*, Chapter 18, RTO Report TR-AVT-113, 2009.

[20-7] Luckring, J.M.: *Reynolds Number, Compressibility, and Leading Edge Bluntness Effects on Delta Wing Aerodynamic*, ICAS 2004 – 24th International Congress of the Aerodynamic Sciences.

[20-8] Breitsamter, Ch.: *Understanding and Modeling Vortical Flows to Improve the Technology Readiness Level for Military Aircraft*, Chapter 21, RTO Report TR-AVT-113, 2009.